

# Coupling of hierarchical fluid models with electrostatic and mechanical models for the dynamic analysis of MEMS

Sudipto K De and N R Aluru

Department of Mechanical Science and Engineering, Beckman Institute for Advanced Science and Technology, University of Illinois at Urbana-Champaign, 405 N. Mathews Avenue, Urbana, IL 61801, USA

E-mail: [aluru@uiuc.edu](mailto:aluru@uiuc.edu)

Received 11 January 2006, in final form 12 June 2006

Published 18 July 2006

Online at [stacks.iop.org/JMM/16/1705](http://stacks.iop.org/JMM/16/1705)

## Abstract

The dynamical behavior of MEMS (micro-electro-mechanical systems) is often strongly affected by viscous fluid/air damping effects from the surrounding. These fluid/air damping effects have to be carefully taken into account during the design and optimization process, in order to get a realistic and reliable description of the device operation. In this paper, two hierarchical fluid models (the 2D compressible Reynold's squeeze film equation and the 2D compressible Navier–Stokes equations) are coupled with a 2D electro-mechanical solver for the dynamic analysis of MEMS to simulate and understand the effect of fluid damping on microstructures. The different physical domains (electrical, mechanical and fluidic) are coupled together using a Newton method for faster convergence. A Lagrangian description of all the physical domains makes it possible to compute the inter-domain coupling terms in the Jacobian matrix of the Newton method exactly. Several MEMS devices (a micromirror, a piggyback actuator, a lateral comb drive and a cantilever beam in air) have been simulated using the coupled electro-mechanical–fluidic solver and numerical results on the resonant frequency and the quality factor are compared with experimental data. The two hierarchical fluid models can be used judiciously (based on speed and accuracy) along with the electro-mechanical solver, depending on the type of MEMS device under consideration, thereby making the dynamic analysis of MEMS devices more efficient.

(Some figures in this article are in colour only in the electronic version)

## 1. Introduction

MEM (micro-electro-mechanical) devices and systems are characterized by very small air gaps (typically a few micrometers) between the moving elements and the fixed parts. As a result, under atmospheric conditions air damping is the dominant energy dissipation mechanism in many mechanical sensors and actuators [1]. Air-packaged MEMS devices are used in a variety of applications such as accelerometers [2], gyroscopes [3] and inertial sensors [4]. In many of these applications, the resonant frequency and the quality factor of the device are the key design parameters which need to be

predicted accurately. Hence, it is important to have a reliable and an efficient physical simulation method that can determine the detailed air flow around these structures and compute the design parameters accurately [5]. Several hierarchical fluid models such as the Reynold's squeeze film equation [6–8], the incompressible Stokes equations [9] and the Navier–Stokes equations [10] have already been used to study fluid damping in MEMS. The fluidic analysis is in general performed on the deformed configuration of the fluid domain and a relaxation scheme is used for self-consistency between the different physical domains, namely electrical, mechanical and fluidic energy domains. Consequently, there is a need to update the

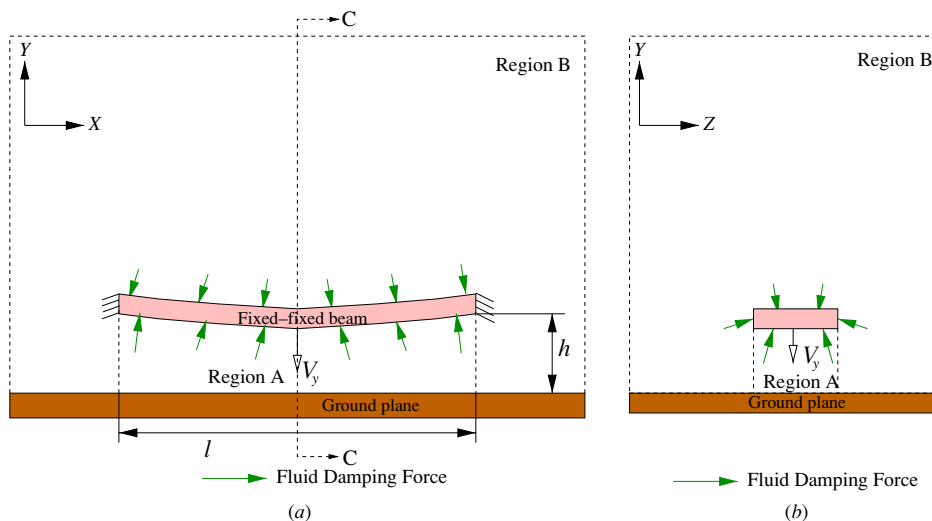


**Figure 1.** Illustration of coupling between the mechanical and fluidic domains in electrostatic MEMS through an example—a MEMS fixed–fixed beam moving with a peak velocity  $V_y$  towards a ground plane giving rise to a fluid flow and the air/fluid damping force acting on it: (a) front view (in the  $X$ – $Y$  plane) and (b) side view (in the  $Y$ – $Z$  plane at section  $CC$ ).

geometry of the fluid domain during each relaxation iteration in each time step. This in turn requires remeshing of the domain and recomputation of the interpolation functions used in the numerical method. Besides, the nonlinear coupling between the different domains can significantly lower the convergence rate of the relaxation scheme (for example, near pull-in conditions in the electro-mechanical coupling case [11–14]) thereby indicating the need for Newton based methods for such tightly coupled cases. The accurate computation of the inter-domain coupling terms in the Jacobian matrix of the Newton method is difficult in the conventional semi-Lagrangian approaches where the mechanical analysis is performed on the undeformed geometries and the electrostatic and fluidic analyses are performed on the deformed geometries. A full-Lagrangian formulation for the electro-mechanical coupling case, in the absence of fluid damping, has already been developed [14–16] and the accurate computation of the Jacobian matrix for this case has been presented in [14].

In this paper, two different fluid models (the compressible Reynold’s squeeze film equation and the compressible Navier–Stokes equations) are coupled with the electrical and the mechanical models using a full-Lagrangian Newton method for the dynamic analysis of MEMS. In [14], a full-Lagrangian Newton method that employs a Lagrangian formulation for both mechanics and electrostatics and a Newton method for self-consistency has been presented. The Lagrangian formulations of the two fluidic models and a Newton method to couple the three physical domains (electrical, mechanical, fluidic) are described in this paper. Exact computation of the inter-domain coupling terms in the Jacobian matrix of the Newton method along with the full-Lagrangian formulation makes the coupled electro-mechanical–fluidic solver robust and efficient. The meshless finite cloud method [17] is used for the interior mechanical and fluidic analyses and the meshless boundary cloud method [18] is used for the exterior electrostatic analysis. Dynamic analysis of several complex MEM devices is performed using the newly developed coupled electro-mechanical–fluidic solver and the numerical results

(resonant frequency and quality factor) are compared with experimental data. For MEMS devices where large aspect ratios and small gaps are present, the compressible Reynold’s squeeze film equation and the compressible Navier–Stokes equations will give identical results [7]. However, as the compressible Reynold’s squeeze film equation (CRSFE) is simpler and faster to solve [7] compared to the compressible Navier–Stokes equations (CNSE), one can select the coupled electro-mechanical–fluidic solver based on CRSFE for such problems. On the other hand, for MEMS devices with large air gaps or complex geometries, CRSFE may not be accurate, in which case the coupled electro-mechanical–fluidic solver based on the CNSE solver can be used for accurate results.

The rest of the paper is outlined as follows: section 2 discusses the theory of fluid damping in MEM devices and the Lagrangian formulations of the governing equations for the different physical domains, section 3 presents the coupling of the fluid models with the electrical and the mechanical models, section 4 presents the results and conclusions are presented in section 5.

## 2. Fluid/air damping in MEMS

The physical coupling between the electrical and the mechanical energy domains in electrostatic MEMS has been described in detail in [14] where fluid damping was not considered. When a surrounding fluid (e.g., air) is present, the movement of the microstructure causes the surrounding fluid to move which in turn gives rise to fluid damping forces acting on the microstructure. The fluid damping force depends on the position and the velocity of the microstructure giving rise to a coupling between the mechanical and the fluidic domains (besides the electro-mechanical coupling that already exists). This coupling between the mechanical and the fluidic domains in MEMS will be explained by considering the generic example shown in figure 1 where a MEMS fixed–fixed beam (microstructure) moves with a peak velocity  $V_y$  towards a ground plane due to some electrostatic force (not

shown in figure 1). The length of the MEMS beam is denoted by  $l$  and its height from the ground plane in the undeformed state is denoted by  $h$  in figure 1. The region exterior to the microstructure is divided into two regions, namely regions A and B, in our discussion. Region A is located between the microstructure and the ground plane. The remaining portion exterior to the microstructure is denoted by region B, as shown in figure 1. When the microstructure moves due to the electrostatic force generated by an applied electrical potential (not shown here), it displaces the surrounding fluid/air. The fluid flow around the microstructure depends on the velocity and the position of the microstructure with respect to the ground plane. The fluid flow in turn gives rise to fluid damping forces that act on the microstructure thereby establishing a coupling between the mechanical and the fluidic domains. If (a) the length of the microstructure  $l$  is sufficiently larger than the height  $h$ , (b) the microstructure is moving perpendicular to the ground plane (as in this case) and (c) the Reynold's number is small, the fluid pressure/velocity variation in region B is minimal and can be neglected [7, 19]. In that case, the fluid damping force can be computed by solving the compressible Reynold's squeeze film equation for region A. For all other cases, where  $l$  and  $h$  are comparable or when the motion of the microstructure is complicated, the compressible Navier–Stokes equations have to be solved in both regions A and B to compute the fluid damping force. Considering all the forces present in the system, at each time instant, the inertial and mechanical stiffness forces (internal forces) are balanced by the external electrostatic and fluidic damping forces. These internal and external forces need to be computed and the position of the microstructure is obtained by considering the balance of all the forces at that time instant. The physical models to compute the various forces are described next.

### 2.1. Mechanical and electrostatic analysis

The mechanical deformation of the MEM structure can be computed by a 2D large deformation elastic analysis of the microstructure. The transient governing equations for an elastic body using a Lagrangian description are given by [20]

$$\rho \ddot{\mathbf{u}} = \nabla \cdot (\mathbf{FS}) \quad \text{in } \Omega, \quad (1)$$

$$\mathbf{u} = \mathbf{G} \quad \text{on } \Gamma_g, \quad (2)$$

$$\mathbf{P} \cdot \mathbf{N} = \mathbf{H} \quad \text{on } \Gamma_h, \quad (3)$$

$$\mathbf{u}|_{t=0} = \mathbf{G}_0 \quad \text{in } \Omega, \quad (4)$$

$$\dot{\mathbf{u}}|_{t=0} = \mathbf{V}_0 \quad \text{in } \Omega. \quad (5)$$

Equation (1) is the governing equation where  $\rho$  is the material density in the undeformed (initial) configuration,  $\mathbf{F}$  is the deformation gradient and  $\mathbf{S}$  is the second Piola–Kirchhoff stress. The differential operator  $\nabla$  is in the undeformed configuration (Lagrangian formulation).  $\mathbf{u}$ ,  $\dot{\mathbf{u}}$  and  $\ddot{\mathbf{u}}$  are the displacement, velocity and acceleration vectors, respectively. Equations (2) and (3) are the displacement and the surface traction boundary conditions, respectively.  $\mathbf{G}$  is the prescribed displacement and  $\mathbf{N}$  is the unit outward normal vector in the initial configuration.  $\mathbf{H}$  is the surface traction on the structure due to the electrostatic and fluid pressures and  $\mathbf{P}$  is the first Piola–Kirchhoff stress tensor. Equations (4) and (5) are the initial conditions for displacement and velocity,

respectively.  $\mathbf{G}_0$  and  $\mathbf{V}_0$  are the prescribed initial displacement and velocity, respectively. A Newmark scheme with an implicit trapezoidal rule (see for example [21] for details) is used to solve the nonlinear dynamical system posed in equations (1)–(5). Numerical discretization is done by using the finite cloud method (FCM) (see [17, 22, 23] for details on FCM).

The 2D governing equation for the electrostatic analysis can be written in a boundary integral form in the Lagrangian frame (see [24] for details)

$$\phi(p(P)) = \int_{d\Omega} \frac{1}{\epsilon} G(p(P), q(Q)) \sigma(q(Q)) \mathbf{J}(Q) d\Gamma_Q + C, \quad (6)$$

$$\int_{d\Omega} \sigma(q(Q)) \mathbf{J}(Q) d\Gamma_Q = C_T, \quad (7)$$

$$\mathbf{J}(Q) = [\mathbf{T}(Q) \cdot \mathbf{C}(Q) \mathbf{T}(Q)]^{\frac{1}{2}}, \quad (8)$$

where  $\epsilon$  is the dielectric constant of the medium,  $\phi$  is the electrostatic potential and  $\sigma$  is the electrostatic surface charge density.  $P$  and  $Q$  are the source and field points in the initial configuration corresponding to the source and field points  $p$  and  $q$  in the deformed configuration and  $G$  is the Green's function. In two dimensions,  $G(p(P), q(Q)) = -\ln|p(P) - q(Q)|/2\pi$ , where  $|p(P) - q(Q)|$  is the distance between the source point  $p(P)$  and the field point  $q(Q)$ .  $C_T$  is the total charge of the system and  $C$  is an unknown variable which can be used to compute the potential at infinity.  $\mathbf{T}(Q)$  is the tangential unit vector at field point  $Q$  and  $\mathbf{C}(Q)$  is the Green deformation tensor. Equations (6)–(8) are solved using the boundary cloud method (BCM) (see [18, 25] for details on BCM) to obtain the distribution of surface charge density,  $\sigma$ , on the conductors. The electrostatic pressure normal to the surface of the conductors is given by

$$P_e = \frac{\sigma^2}{2\epsilon}. \quad (9)$$

### 2.2. Fluidic analysis

As discussed in the beginning of this section, depending on the thickness of the fluid gap  $h$  and the direction of motion of the microstructure, fluidic analysis can be simplified (compared to solving the more complicated compressible Navier–Stokes equations) by solving the compressible Reynold's squeeze film equation. In this section, the governing equations for both the fluidic analyses are presented. The 2D compressible Navier–Stokes equations have been used to compute fluid damping forces for large air gaps and for non-trivial geometries in this paper.

2.2.1. *Compressible Reynold's squeeze film equation (CRSFE)*. The isothermal Reynold's squeeze film equation for a compressible slip flow is given by [6, 26]

$$\frac{\partial}{\partial x} \left[ (1 + 6K) h^3 P_f \frac{\partial P_f}{\partial x} \right] + \frac{\partial}{\partial z} \left[ (1 + 6K) h^3 P_f \frac{\partial P_f}{\partial z} \right] = 12\eta \frac{\partial(P_f h)}{\partial t}, \quad (10)$$

where  $h$  is the gap between the movable structure and the ground electrode of the MEM device (same as the fluid film

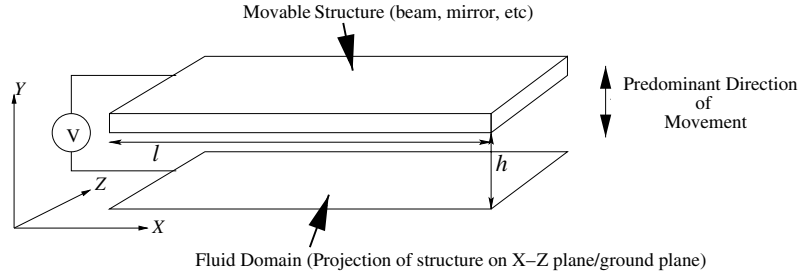


**Figure 2.** Structural and fluidic domains for Reynold's squeeze film damping analysis.

thickness),  $P_f$  is the fluid pressure under the structure (region A in figure 1) and  $\eta$  is the viscosity of the surrounding fluid.  $K = \lambda/h$  is the Knudsen number, where  $\lambda$  is the mean free path of the surrounding fluid. The rarefaction/slip flow effects present in the system due to the small device dimensions and/or low ambient pressures are taken into account by the term  $1 + 6K$  in equation (10). This correction term for the isothermal Reynold's squeeze film equation was derived in [26] by assuming first-order slip flow boundary conditions and is valid up to  $K = 1$ . Several other models for the correction term have been discussed in [27] (some are based on the linearized Boltzmann equation and valid up to  $K = 880$  [7]). The variation of the fluid pressure,  $P_f$ , in the height direction ( $Y$ -direction in figures 1 and 2) is assumed to be negligible in CRSFE [19]. As a result, the fluid domain where the Reynold's squeeze film equation is solved (for region A in figure 1) is the projection of the MEM structure on the  $X$ - $Z$  plane (ground plane) [6] as shown in figure 2. As the moving structure deforms due to the application of an external electric field, the projected fluid domain also changes. Equation (10) is written in the deformed configuration (projected fluid domain) which varies with time ( $x$  and  $z$  are the coordinates in the deformed configuration). A Lagrangian form of equation (10) is developed in this paper:

$$\frac{\partial}{\partial X} \left[ (1 + 6K)h^3 P_f \frac{\partial P_f}{\partial X} \left( 1 + \frac{\partial u}{\partial X} \right)^{-1} \right] \left( 1 + \frac{\partial u}{\partial X} \right)^{-1} + \frac{\partial}{\partial Z} \left[ (1 + 6K)h^3 P_f \frac{\partial P_f}{\partial Z} \right] = 12\eta \frac{\partial(P_f h)}{\partial t}, \quad (11)$$

where  $X, Z$  are the coordinates of the fluid domain corresponding to the undeformed state of the movable structure and  $u$  is the deformation of the movable structure in the  $X$ -direction. As the 2D mechanical equations are solved in the  $X$ - $Y$  domain, mechanical deformation and its variation in the  $Z$ -direction are assumed to be zero. The fluid pressure,  $P_f$ , obtained from equation (11) is integrated along the  $Z$ -direction to compute an effective fluid pressure,  $P_{fe}$ , which is applied as a boundary condition in the 2D mechanical analysis in the  $X$ - $Y$  domain [6].

The mean free path,  $\lambda$  (used for computing  $K$  in equation (11)), is related to the ambient temperature and pressure by the relation [28]

$$\lambda = \frac{k_B T}{\sqrt{2\pi} p d^2}, \quad (12)$$

where  $k_B$  is the Boltzmann constant,  $T$  is the absolute temperature,  $p$  is the ambient pressure and  $d$  is the collision diameter of the fluid molecules ( $d = 3.66 \text{ \AA}$  for air [28]).

The effective fluid pressure,  $P_{fe}$ , from the fluidic analysis and the electrostatic pressure,  $P_e$ , obtained from the electrostatic analysis (equation (9)) are used to compute  $\mathbf{H}$  in equation (3) using

$$\mathbf{H} = J(P_e - P_{fe})\mathbf{F}^{-T}\mathbf{N}, \quad (13)$$

where  $J = \det(\mathbf{F})$ . A self-consistent solution of the coupled electro-mechanical–fluidic analysis at each time step is obtained using a Newton method as discussed in section 3. The time integration scheme and the numerical discretization of equation (11) are given in appendix A.

**2.2.2. Compressible Navier–Stokes equations (CNSE).** A more general method to determine the fluid damping forces is to use the compressible Navier–Stokes equations. A Lagrangian form of the compressible Navier–Stokes equations (assuming a Newtonian viscous fluid) can be written as [29]

$$\frac{\partial \rho_f J_f}{\partial t} = 0, \quad (14)$$

$$\frac{\partial \rho_f J_f \mathbf{u}_f}{\partial t} - \nabla \cdot (J_f \mathbf{T}_f \mathbf{F}_f^{-T}) = 0, \quad (15)$$

where  $\rho_f$  is the fluid density,  $\mathbf{u}_f$  is the fluid velocity vector,  $\mathbf{F}_f = \mathbf{I} + \nabla \mathbf{x}_f$  is the deformation gradient of the fluid ( $\mathbf{x}_f$  is the displacement vector of the fluid) and  $J_f = \det(\mathbf{F}_f)$ .  $\mathbf{T}_f$  is the fluidic stress tensor in the deformed configuration given by

$$\mathbf{T}_f = -P_f \mathbf{I} + \begin{bmatrix} \sigma_{xx} & \tau_{xy} \\ \tau_{yx} & \sigma_{yy} \end{bmatrix}, \quad (16)$$

where  $\mathbf{I}$  is the  $2 \times 2$  identity matrix.  $\sigma_{xx}$ ,  $\tau_{xy}$ ,  $\tau_{yx}$  and  $\sigma_{yy}$  are the viscous stress terms in the deformed configuration of the fluid.

There are several advantages of using a Lagrangian formulation over a conventional Eulerian formulation for the compressible Navier–Stokes equations (CNSE). In the Lagrangian formulation, the fluid and the solid points/meshes at the solid–fluid interface remain fixed at all time instants, as a result of which the transfer of boundary conditions from mechanics to fluidics and vice versa can be done accurately and easily [30]. This also allows the exact computation of the mechanical to fluidic and fluidic to mechanical coupling terms of the Jacobian matrix in the Newton method. Besides, once the equations are mapped back to the original undeformed fluid domain/coordinate system (equations (14) and (15)), discretization of the deformed fluid domain and recomputation of the interpolation functions for the deformed fluid domain are eliminated. In this paper, a Lagrangian form of the 2D compressible Navier–Stokes equations is

implemented. Equations (14) and (15), after symmetrization [31], when solved in the  $X$ - $Y$  coordinate system (see figure 1) can be written as

$$\frac{\partial(\rho_f J_f)}{\partial t} - \frac{\partial}{\partial X}(u_f M - v_f L) - \frac{\partial}{\partial Y}(v_f A - u_f B) = 0, \quad (17)$$

$$\begin{aligned} \frac{\partial(\rho_f J_f u_f)}{\partial t} + \frac{\partial}{\partial X}(P_f M - \sigma_{xx} M + \tau_{xy} L) \\ + \frac{\partial}{\partial Y}(-P_f B + \sigma_{xx} B - \tau_{xy} A) = 0, \end{aligned} \quad (18)$$

$$\begin{aligned} \frac{\partial(\rho_f J_f v_f)}{\partial t} + \frac{\partial}{\partial X}(-P_f L - \tau_{yx} M + \sigma_{yy} L) \\ + \frac{\partial}{\partial Y}(P_f A + \tau_{yx} B - \sigma_{yy} A) = 0, \end{aligned} \quad (19)$$

where the geometrical terms  $A$ ,  $B$ ,  $L$  and  $M$  (the components of the deformation gradient  $\mathbf{F}_f$ ) are obtained using the relations

$$\begin{aligned} \frac{\partial A}{\partial t} - \frac{\partial u_f}{\partial X} = 0, \quad \frac{\partial B}{\partial t} - \frac{\partial v_f}{\partial X} = 0, \\ \frac{\partial L}{\partial t} - \frac{\partial u_f}{\partial Y} = 0, \quad \frac{\partial M}{\partial t} - \frac{\partial v_f}{\partial Y} = 0. \end{aligned} \quad (20)$$

$P_f$  is the fluid pressure and  $u_f$  and  $v_f$  are the fluid velocities in the  $X$  and  $Y$  directions, respectively. The ideal gas equation,  $P_f = \rho_f R T$ , is used to relate the density of the fluid with the pressure (for air) and isothermal conditions are assumed.  $R$  is the gas constant and  $T$  is the absolute temperature.  $\sigma_{xx}$ ,  $\tau_{xy}$ ,  $\tau_{yx}$  and  $\sigma_{yy}$  (viscous stress terms in the deformed configuration) can be expressed in the Lagrangian frame as

$$\begin{aligned} \sigma_{xx} &= \frac{2\eta}{3} \left[ 2 \frac{\partial u_f}{\partial x} - \frac{\partial v_f}{\partial y} \right] \\ &= \frac{2\eta}{3} \left[ \frac{2M}{J_f} \frac{\partial u_f}{\partial X} - \frac{2B}{J_f} \frac{\partial u_f}{\partial Y} + \frac{L}{J_f} \frac{\partial v_f}{\partial X} - \frac{A}{J_f} \frac{\partial v_f}{\partial Y} \right], \end{aligned} \quad (21)$$

$$\begin{aligned} \tau_{xy} = \tau_{yx} &= \eta \left[ \frac{\partial u_f}{\partial y} + \frac{\partial v_f}{\partial x} \right] \\ &= \eta \left[ -\frac{L}{J_f} \frac{\partial u_f}{\partial X} + \frac{A}{J_f} \frac{\partial u_f}{\partial Y} + \frac{M}{J_f} \frac{\partial v_f}{\partial X} - \frac{B}{J_f} \frac{\partial v_f}{\partial Y} \right], \end{aligned} \quad (22)$$

$$\begin{aligned} \sigma_{yy} &= \frac{2\eta}{3} \left[ 2 \frac{\partial v_f}{\partial y} - \frac{\partial u_f}{\partial x} \right] \\ &= \frac{2\eta}{3} \left[ -\frac{M}{J_f} \frac{\partial u_f}{\partial X} + \frac{B}{J_f} \frac{\partial u_f}{\partial Y} - \frac{2L}{J_f} \frac{\partial v_f}{\partial X} - \frac{2A}{J_f} \frac{\partial v_f}{\partial Y} \right], \end{aligned} \quad (23)$$

where  $\eta$  is the viscosity of the fluid.

The coupling between the solid (microstructure) and the fluid is realized through standard boundary conditions at the fluid–microstructure interface, namely the kinematic conditions [29], expressing the continuity of velocity and the continuity of stress. However, some of the MEMS devices simulated in this paper are in the slip flow regime (i.e.,  $0.01 \geq K \geq 0.1$ ) where the rarefaction effects are modeled through the first-order slip flow boundary condition [1] at the fluid–microstructure interface (same approximation as that used in equation (10)),

$$u_s - u_w = K \frac{\partial u_s}{\partial \mathbf{n}} = K \left( \mathbf{F}_f^{-T} \nabla u_s \cdot \frac{\mathbf{F}_f^{-T} \mathbf{N}}{|\mathbf{F}_f^{-T} \mathbf{N}|} \right), \quad (24)$$

where  $u_s$  is the tangential velocity of the fluid at the fluid–microstructure interface and  $u_w$  is the tangential microstructure velocity at that point and  $K$  is the Knudsen number.  $\mathbf{n}$  and  $\mathbf{N}$  denote the outward unit normal vector at the wall/fluid–microstructure interface in the deformed and the undeformed configurations, respectively. The fluidic stress,  $\mathbf{T}_f$ , obtained from the fluidic analysis and the electrostatic pressure,  $P_e$ , obtained from the electrostatic analysis (equation (9)) are used to compute  $\mathbf{H}$  in equation (3) using the relation

$$\mathbf{H} = J [P_e \mathbf{I} + \mathbf{T}_f] \mathbf{F}^{-T} \mathbf{N}. \quad (25)$$

A self-consistent solution of the coupled electro-mechanical–fluidic analysis at each time step is obtained using a Newton method discussed in section 3. The time integration scheme and the numerical discretization of equations (17)–(20) are given in appendix B.

### 3. Coupling of the fluid models with the electrostatic and mechanical models

In the full-Lagrangian formulation, since the mechanical, electrical and the fluidic analyses are all done on the original undeformed geometry, the inter-domain coupling terms in the Jacobian matrix can be computed directly (i.e., they can be expressed mathematically in a closed form) and, hence, a Newton method that can exhibit higher convergence rate and robustness can be developed. The two hierarchical models for fluid damping are coupled with the electro-mechanical solver presented in [14] using a full-Lagrangian formulation and a Newton scheme, as discussed in this section. The full-Lagrangian Newton scheme is much more efficient and robust than existing coupled solvers for MEMS dynamics because of the following reasons [14]:

- (i) A full-Lagrangian formulation eliminates rediscrretization of the geometry and recomputation of interpolation functions used in the numerical method during each Newton iteration in each time step of the dynamic simulations.
- (ii) A direct Newton method with accurate computation of the Jacobian matrix gives faster convergence and robustness.

The basic step in the Newton method for the coupled electro-mechanical–fluidic analysis involves solving the equation

$$\begin{aligned} \bar{\mathbf{J}}(\mathbf{x}) \Delta \mathbf{x} &= -\mathbf{r}(\mathbf{x}), \\ \text{i.e.} \quad \begin{bmatrix} \mathbf{R}_{MM} & \mathbf{R}_{ME} & \mathbf{R}_{MF} \\ \mathbf{R}_{EM} & \mathbf{R}_{EE} & \mathbf{R}_{EF} \\ \mathbf{R}_{FM} & \mathbf{R}_{FE} & \mathbf{R}_{FF} \end{bmatrix} \begin{Bmatrix} \Delta \mathbf{x}_M \\ \Delta \mathbf{x}_E \\ \Delta \mathbf{x}_F \end{Bmatrix} &= - \begin{Bmatrix} \mathbf{R}_M \\ \mathbf{R}_E \\ \mathbf{R}_F \end{Bmatrix}, \end{aligned} \quad (26)$$

in each time step of the dynamic analysis.  $\bar{\mathbf{J}}$  is the Jacobian matrix and the subscripts M, E and F denote mechanical, electrical and fluidic domains, respectively. In equation (26),  $\mathbf{R}_{ME}$  denotes the electrical (E) to mechanical (M) coupling term in the Jacobian matrix. The other terms in  $\bar{\mathbf{J}}$  are defined similarly.  $\mathbf{x}$  is the vector of unknown variables where  $\mathbf{x}_M$ ,  $\mathbf{x}_E$  and  $\mathbf{x}_F$  are the mechanical, electrical and fluidic variables, respectively. For the 2D mechanical and electrical analyses implemented in this paper,  $\mathbf{x}_M = \{u, v\}^T$ , where  $u$  and  $v$  are the displacements of the microstructure in the  $X$  and  $Y$  directions, respectively, and  $\mathbf{x}_E = \{\sigma, C\}^T$ . The fluidic variables  $\mathbf{x}_F = \{P_f\}$  for the 2D CRSFE, and for the 2D CNSE,

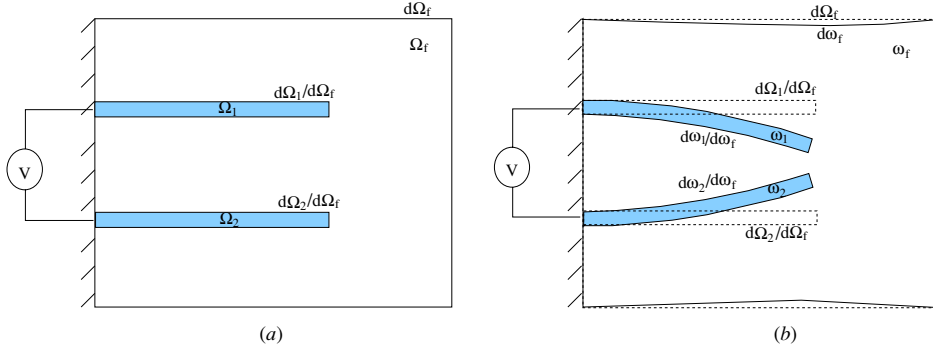


**Figure 3.** (a) Undeformed and (b) deformed configurations of the mechanical (two cantilever beams), electrical (cantilever beam surfaces) and fluidic (surrounding air) domains in a two-conductor MEMS system.

$\mathbf{x}_F = \{\rho_f, u_f, v_f, A, B, L, M\}^T$ . The mechanical, electrical and fluidic residual equations are denoted by  $\mathbf{R}_M$ ,  $\mathbf{R}_E$  and  $\mathbf{R}_F$ , respectively, in equation (26). The expressions for  $\mathbf{R}_M$  and  $\mathbf{R}_E$  are described in detail in [14].

The full-Lagrangian Newton scheme (for both the fluid damping cases) is presented in detail in algorithm 1. Algorithm 1 is discussed with reference to the two-conductor system shown in figure 3. In figure 3,  $\Omega_1$  and  $\Omega_2$  denote the original/undeformed geometries and  $d\Omega_1$  and  $d\Omega_2$  denote the original/undeformed surfaces/boundaries of conductors 1 and 2, respectively, where the mechanical analysis is done.  $\Omega_f$  denotes the original/undeformed geometry and  $d\Omega_f$  denotes the original/undeformed boundaries of the fluid domain (for fluidic analysis). The electrostatic analysis is done on the original/undeformed surfaces/boundaries of conductors 1 and 2, namely  $d\Omega_1$  and  $d\Omega_2$ , respectively. A potential difference  $V$  is applied between conductors 1 and 2 which deforms the conductors.  $\omega_1$  denotes the deformed shape of conductor 1,  $\omega_2$  denotes the deformed shape of conductor 2 and  $\omega_f$  denotes the deformed shape of the fluid domain.  $d\omega_1$ ,  $d\omega_2$  and  $d\omega_f$  denote the deformed surfaces/boundaries of conductors 1, 2 and the fluid domain, respectively. The applied potential does not change as the conductors undergo deformation or shape changes. In algorithm 1, the index  $n$  stands for the time instant whereas the index  $i$  denotes the  $i$ th Newton iteration within the time step  $n$ .  $\text{tol}$  is some specified tolerance for checking the convergence of the Newton scheme. Once the domains are discretized, the mechanical, electrical and fluidic unknowns are initialized (set to zero for our case). In each time step, a Newton scheme is implemented to obtain a self-consistent solution for that time step. The initial guesses for the Newton method are generally taken to be the final solutions of the previous time step. The computation of the terms  $\mathbf{R}_{MM}$ ,  $\mathbf{R}_{ME}$ ,  $\mathbf{R}_{EM}$  and  $\mathbf{R}_{EE}$ , the mechanical and electrical variables ( $\mathbf{x}_M$ ,  $\mathbf{x}_E$ ) and the residual equations ( $\mathbf{R}_M$ ,  $\mathbf{R}_E$ ) in equation (26) are all described in detail in [14]. Further,  $\mathbf{R}_{EF} = \mathbf{R}_{FE} = 0$ , i.e., there exists no coupling between the electrical and fluidic domains. The computation of the terms  $\mathbf{R}_{MF}$ ,  $\mathbf{R}_{FM}$  and  $\mathbf{R}_{FF}$ , the fluidic residual equation  $\mathbf{R}_F$  and the fluidic variables  $\mathbf{x}_F$  for the two different fluid models, namely the compressible Reynold's squeeze film equation and the compressible Navier–Stokes equations, are described in appendices A and B, respectively.

**Algorithm 1** Full-Lagrangian Newton scheme for the self-consistent dynamic analysis of MEMS.

1. Define  $\Omega_1, d\Omega_1, \Omega_2, d\Omega_2, \Omega_f, d\Omega_f$
2. Discretize  $\Omega_1, \Omega_2, \Omega_f$  for mechanical and fluidic analysis
3. Discretize  $d\Omega_1, d\Omega_2$  for electrostatic analysis
4. Set  $n = 0, t^n = t^0 = 0$
5. Initialize  $\mathbf{x}_M(t^n), \mathbf{x}_E(t^n), \mathbf{x}_F(t^n)$
6. For  $n = 0, 1, 2, \dots, N$ :

- 6(a). Set  $i = 0$
- 6(b). Set  $\mathbf{x}_M(t_i^{n+1}) = \mathbf{x}_M(t_i^n), \mathbf{x}_E(t_i^{n+1}) = \mathbf{x}_E(t_i^n), \mathbf{x}_F(t_i^{n+1}) = \mathbf{x}_F(t_i^n)$

**repeat**

- A. Compute  $\bar{\mathbf{J}}(t_i^{n+1}) = \bar{\mathbf{J}}(\mathbf{x}_M(t_i^{n+1}), \mathbf{x}_E(t_i^{n+1}), \mathbf{x}_F(t_i^{n+1}))$
- B. Compute  $\mathbf{r}(t_i^{n+1}) = \mathbf{r}(\mathbf{x}_M(t_i^{n+1}), \mathbf{x}_E(t_i^{n+1}), \mathbf{x}_F(t_i^{n+1}))$
- C. Solve  $\bar{\mathbf{J}}(t_i^{n+1})[\Delta\mathbf{x}_M(t_i^{n+1}) \Delta\mathbf{x}_E(t_i^{n+1}) \Delta\mathbf{x}_F(t_i^{n+1})] = -\mathbf{r}(t_i^{n+1})$  (equation (26))
- D. Update  $\mathbf{x}_M(t_{i+1}^{n+1}) = \mathbf{x}_M(t_i^{n+1}) + \Delta\mathbf{x}_M(t_i^{n+1}), \mathbf{x}_E(t_{i+1}^{n+1}) = \mathbf{x}_E(t_i^{n+1}) + \Delta\mathbf{x}_E(t_i^{n+1}), \mathbf{x}_F(t_{i+1}^{n+1}) = \mathbf{x}_F(t_i^{n+1}) + \Delta\mathbf{x}_F(t_i^{n+1})$
- E. Update  $i = i + 1$

**until**  $|\Delta\mathbf{x}_M(t_{i+1}^{n+1})| < \text{tol}$  and  $|\Delta\mathbf{x}_E(t_{i+1}^{n+1})| < \text{tol}$  and  $|\Delta\mathbf{x}_F(t_{i+1}^{n+1})| < \text{tol}$

- 6(c). Update  $\mathbf{x}_M(t^{n+1}) = \mathbf{x}_M(t_{i+1}^{n+1}), \mathbf{x}_E(t^{n+1}) = \mathbf{x}_E(t_{i+1}^{n+1})$  and  $\mathbf{x}_F(t^{n+1}) = \mathbf{x}_F(t_{i+1}^{n+1})$
- 6(d). End of for loop  $n$

## 4. Results

The full-Lagrangian Newton scheme described in section 3 for coupled electro-mechanical–fluidic analysis is applied in this section for the dynamic analysis of several complex MEMS devices. Important design parameters such as resonant frequency and quality factor are computed for these devices and compared with experimental data to validate the physical models.

### 4.1. Micromirror

The first device considered is a MEMS torsion mirror [8] shown in figure 4. The mirror plate is  $1500 \mu\text{m}$  long,  $1400 \mu\text{m}$  wide and  $3 \mu\text{m}$  thick. Four  $150 \mu\text{m}$  long electrodes (of negligible thickness) are attached to the mirror plate and the ground plane. The distance from the center of the

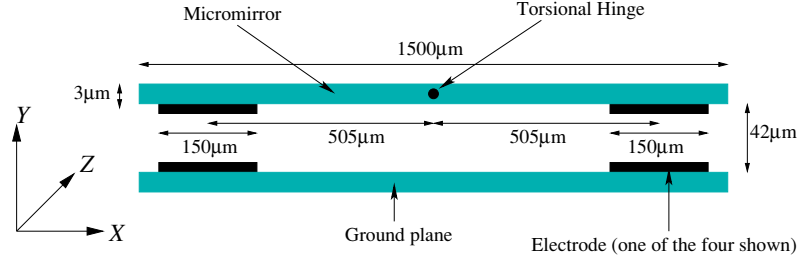


Figure 4. MEMS torsion mirror [8].

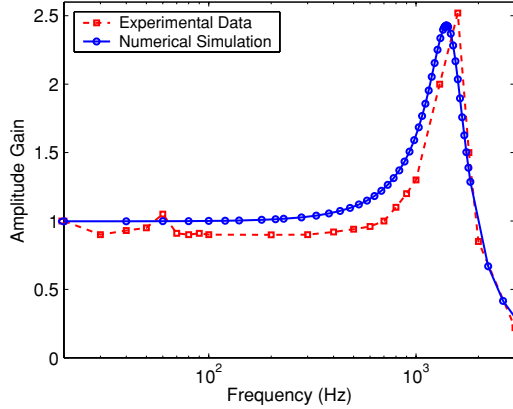


Figure 5. Frequency response of the MEMS torsion mirror under an external torque  $T_e = 4.84 \times 10^{-9} \sin(2\pi ft)$  N m.

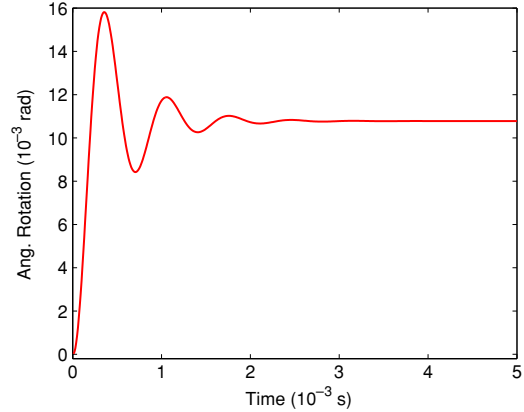


Figure 6. Transient response of the MEMS torsion mirror for a constant external torque  $T_e = 4.84 \times 10^{-9}$  N m.

electrodes on the mirror to the center of the mirror is  $505 \mu\text{m}$ . The gap between the mirror and the ground plane is  $42 \mu\text{m}$ .  $I_\theta = 5.51 \times 10^{-15} \text{ kg m}^2$  is the moment of inertia of the mirror and  $K_\theta = 4.49 \times 10^{-7} \text{ N m rad}^{-1}$  is the torsional stiffness of the mirror. Squeeze film damping between the mirror and the ground electrode is the dominant dissipative mechanism for this device and has been solved using the coupled electro-mechanical–fluidic solver based on 2D CRSFE in the  $X$ – $Z$  plane for the fluidic analysis. An external torque  $T_e = 4.84 \times 10^{-9} \sin(2\pi ft)$  N m where  $f$  is the frequency in Hz is applied in the absence of any electrode voltages to the torsion mirror at 1 atm ( $1.013 \times 10^5$  Pa). The viscosity is  $\eta = 1.82 \times 10^{-5} \text{ kg m}^{-1} \text{ s}^{-1}$  and the mean free path  $\lambda$  for air is computed from equation (12) at 1 atm and 293 K. The frequency response curve of the torsion mirror under the external torque  $T_e$  is shown in figure 5. The transient response of the mirror under a constant external torque  $T_e = 4.84 \times 10^{-9}$  N m is shown in figure 6. The simulated resonant frequency and the damping ratio  $\zeta = \frac{1}{2Q}$  ( $Q$  is the quality factor) of the mirror are 1.41 kHz and 0.20, respectively. The corresponding experimental values are 1.59 kHz and 0.19. The simulated and experimental damping ratios (which primarily depend on the geometry and the ambient pressure) match well. However, there is some difference between the simulated and experimental resonant frequencies. This can be attributed to the fact that the mirror surface is assumed to be rigid in the simulations thereby neglecting any elastic deformation effect of the surface [8]. Besides, experimental measurements can also have errors. For example, it is very difficult to accurately measure the gap between the mirror and the ground plane (an

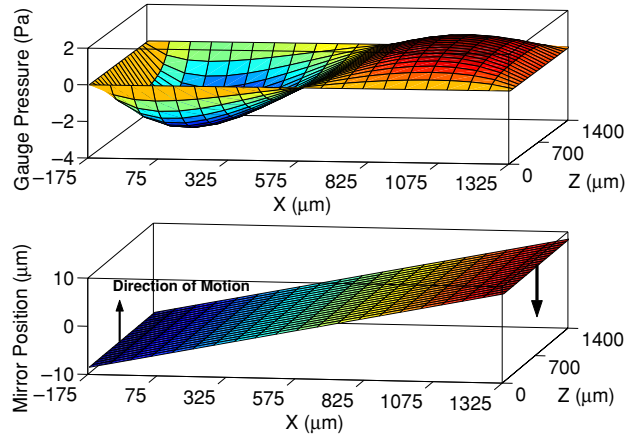


Figure 7. Pressure profile in the gap at a given time instant.

error of 5% can be present using conventional measurement techniques [32]). Figure 7 shows the fluid pressure profile in the gap between the mirror and the ground plane for a particular position of the mirror at a given time instant.

#### 4.2. Piggyback actuator

Figure 8 shows a MEMS piggyback actuator for hard-disk drive applications [33]. The actuator consists of a movable mass suspended by two restoring springs. The restoring springs are  $500 \mu\text{m}$  long and  $18 \mu\text{m}$  wide. The movable mass has 11 electrodes (movable electrodes) on it. Each

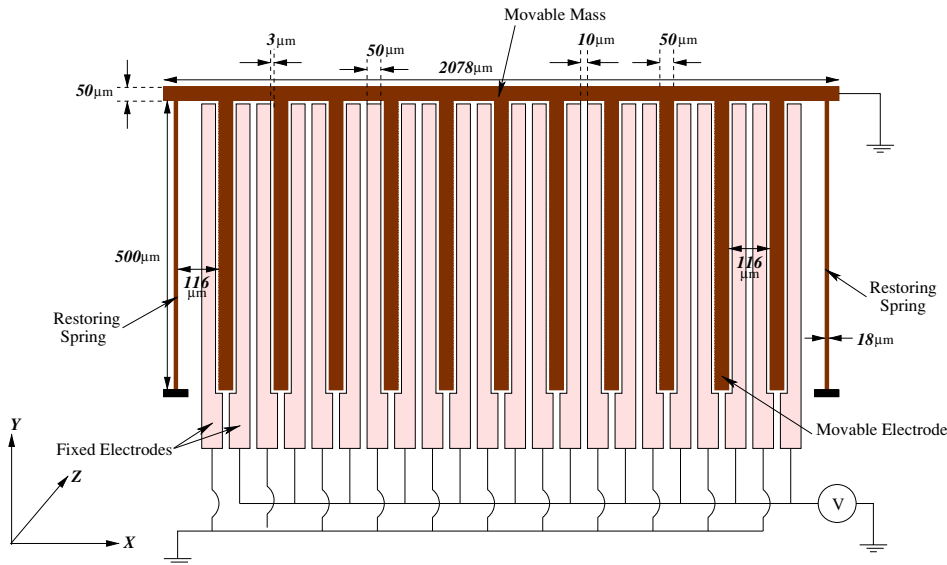


Figure 8. A MEMS piggyback actuator [33]. The actuator moves in the  $X$ -direction.

movable electrode has two fixed electrodes—one on either side. One of the fixed electrode is grounded and a potential is applied on the other electrode as shown in figure 8. The movable electrodes are  $500 \mu\text{m}$  long and  $50 \mu\text{m}$  wide and the overlap length between the fixed and the movable electrodes is  $498 \mu\text{m}$ . The gap between the movable and the fixed electrodes on either side is  $3 \mu\text{m}$ . The length of the movable mass is  $2078 \mu\text{m}$ . The height (normal to the plane of the paper) of the structure is  $50 \mu\text{m}$ . The whole structure is made from silicon and has a Young's modulus  $E = 140 \text{ GPa}$ , density  $\rho = 2330 \text{ kg m}^{-3}$  and Poisson's ratio  $\nu = 0.3$  [33]. Squeeze film damping in the narrow air gaps between the movable electrodes and the fixed electrodes is the dominant dissipative mechanism for this device. The device is simulated using the coupled electro-mechanical–fluidic solver based on 2D CRSFE for the fluidic analysis. The viscosity of air is taken to be  $\eta = 1.82 \times 10^{-5} \text{ kg m}^{-1} \text{ s}^{-1}$  and the mean free path  $\lambda$  for air is computed from equation (12) at 1 atm and 293 K. The 2D CRSFE simulation is done for the narrow air gaps between the movable electrodes and the fixed electrodes in the  $Y$ - $Z$  plane ( $498 \mu\text{m}$  in the  $Y$ -direction and  $50 \mu\text{m}$  in the  $Z$ -direction). Figure 9(a) shows the pressure profile in the air gap between the electrodes at a given time instant ( $t = 20 \mu\text{s}$ ) obtained using the 2D CRSFE solver. As the overlap length of the fingers along the  $Y$ -direction ( $498 \mu\text{m}$ ) is much larger than the width of the fingers in the  $Z$ -direction ( $50 \mu\text{m}$ ), the pressure variation along the  $Y$ -direction is negligible compared to the pressure variation along the  $Z$ -direction. As a result, the 2D CNSE based solver simulated in the  $X$ - $Z$  plane is expected to give similar results as the 2D CRSFE solver in the  $Y$ - $Z$  plane. While the 2D CNSE solver in the  $X$ - $Z$  plane is equivalent to the 3D CNSE in this case due to negligible variations in the  $Y$ -direction, the 2D CRSFE in the  $Y$ - $Z$  plane is also equivalent to the 3D CNSE in this case due to the narrow air gap between the electrodes. The pressure profile in the air gap between the electrodes at the given time instant ( $t = 20 \mu\text{s}$ ) obtained using the 2D CNSE solver in the  $X$ - $Z$  plane is shown in figure 9(b). Figure 9(b) shows that the pressure variation

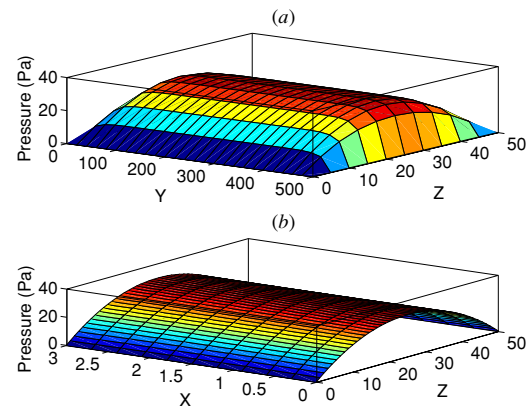
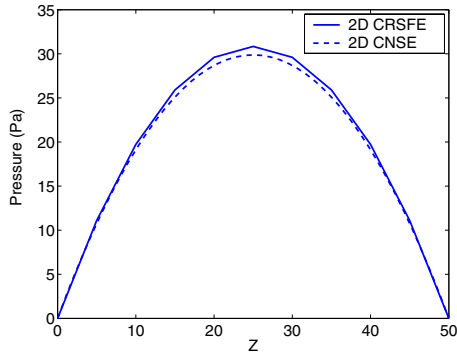


Figure 9. Pressure profile in the air gaps between the electrodes of the piggyback actuator at a given time instant ( $t = 20 \mu\text{s}$ ) obtained using (a) the 2D CRSFE solver in the  $Y$ - $Z$  domain and (b) the 2D CNSE solver in the  $X$ - $Z$  domain.

in the  $X$ -direction (in the height direction of the electrodes) is negligible. This is an important assumption in the derivation of the 2D CRSFE from 3D CNSE and is found to be true. Figure 10 compares the pressure profile in the  $Z$ -direction in the air gaps between the electrodes of the piggyback actuator at the given time instant ( $t = 20 \mu\text{s}$ ) obtained using the 2D CRSFE solver (plotted at the centerline  $Y = 249 \mu\text{m}$ ) and the 2D CNSE solver (plotted at the centerline  $X = 1.5 \mu\text{m}$ ). The pressure profiles given by the two solvers are in good agreement.

Figure 11 shows the damped transient response of the rigid movable mass of the MEMS piggyback actuator under a 25 V dc bias. Both the solvers (the 2D CRSFE and the 2D CNSE) are found to give very similar results (as expected from the above discussion). The frequency response of the piggyback actuator at 20 V dc and 5 V ac (ac voltage of the form  $V_{ac} \sin(2\pi ft)$ ) is simulated using the coupled electro-mechanical–fluidic solver based on 2D CRSFE for the fluidic



**Figure 10.** Pressure variation in the Z-direction in the air gaps between the electrodes of the piggyback actuator at the given time instant ( $t = 20 \mu\text{s}$ ) using the 2D CRSFE solver (plotted at the centerline  $Y = 249 \mu\text{m}$ ) and the 2D CNSE solver (plotted at the centerline  $X = 1.5 \mu\text{m}$ ).

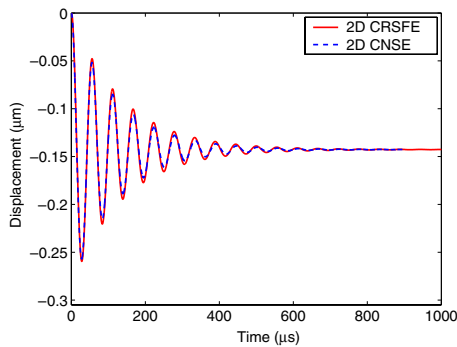


**Figure 11.** Damped transient response of the rigid movable mass of the MEMS piggyback actuator at 25 V dc.

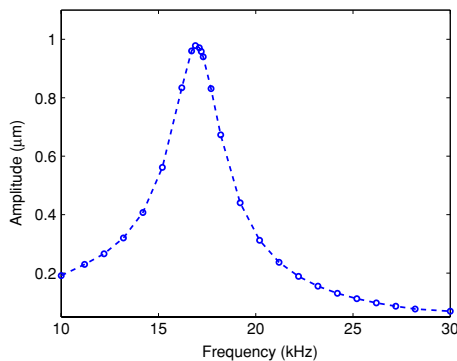


**Figure 12.** Frequency response of the MEMS piggyback actuator at 20 V dc and 5 V ac using 2D CRSFE for fluid damping.

analysis and is shown in figure 12. The resonant frequency and the quality factor of the piggyback actuator are found to be 16.8 kHz and 7.52, respectively, from the frequency response plot. The corresponding experimental values are 16 kHz for the resonant frequency and 7.73 for the quality factor. The experimental data are close to the simulated results.

#### 4.3. Lateral comb drive

Comb drives are an important class of MEM devices as they have numerous applications ranging from micro-accelerometers, position controllers to hard-disk drive

actuators [34–36]. Consequently, dynamic characterization of these devices is very important for efficient design and development. Figure 13 shows a laterally driven comb drive in air [36]. The system consists of a movable center stage, four pairs of interdigitated teeth (combs) and two spring beams. The center stage is supported by the two folded spring beams anchored at the ends. The four combs consist of a driving comb, a sensing comb and two secondary combs. Electrostatic forces are generated when a voltage is applied between the fixed and movable electrodes/fingers of the drive comb and the displacement of the movable stage is obtained by measuring the change in capacitance between the fixed and movable electrodes/fingers of the sensing comb. The fluid damping due to the fingers in the secondary combs is simulated and compared with experimental results. The spring beams are 200  $\mu\text{m}$  long and 2  $\mu\text{m}$  wide and the center stage is 230  $\mu\text{m}$  long and 30  $\mu\text{m}$  wide. All the four combs are identical with 20 pairs of movable and fixed fingers/electrodes in each. The fingers are 40  $\mu\text{m}$  long and 2  $\mu\text{m}$  wide and the overlap length between the fixed and the movable fingers is 14  $\mu\text{m}$ . The comb gap (gap between fixed and movable fingers) is 2  $\mu\text{m}$  on either side. The central truss on which the secondary combs are mounted is 220  $\mu\text{m}$  long and 10  $\mu\text{m}$  wide. The thickness of the whole structure is 2.1  $\mu\text{m}$ . The movable structure is made from silicon and has a Young's modulus  $E = 140 \text{ GPa}$ , density  $\rho = 2330 \text{ kg m}^{-3}$  and Poisson's ratio  $\nu = 0.3$  [36].

Figure 14 shows the damped transient response of the rigid center stage of the comb drive for a 25 V dc driving voltage. The damping from the secondary comb fingers (inter-comb damping due to the presence of the fixed and movable fingers) is only considered and the coupled electro-mechanical–fluidic solver based on 2D CNSE is used. The 2D CNSE simulation is done in the  $X$ – $Y$  plane for the fluidic analysis. The ambient conditions and the viscosity of air are taken to be the same as in the case of the micromirror and the piggyback actuator. The frequency response curve of the lateral comb drive is plotted in figure 15. The simulations are done for a 20 V dc bias and a 10 V ac signal whose frequency is varied from 6 kHz to 13 kHz. From both figures 14 and 15, the resonant frequency and the quality factor (due to inter-comb damping) are found to be 9.45 kHz and 235, respectively. The experimentally measured resonant frequency is 9.6 kHz and the quality factor due to inter-comb damping is found to be 246 [36], indicating that the simulation results are close to the experimental data. The effects of the finger overlap length (14  $\mu\text{m}$  in the actual device) and the inter-comb gap (2  $\mu\text{m}$  in the actual device) on the quality factor are studied next and the results are presented in figures 16 and 17, respectively. From figure 16, it can be seen that the quality factor decreases with the finger overlap length in a nonlinear manner. On the other hand, from figure 17, it can be seen that the quality factor increases with the comb gap linearly. Since the electrostatic force in lateral comb drives depends only on the comb gap and is independent of the finger overlap length [37], for high quality factor operation, the finger overlap length should be kept as small as possible and an optimum value of the comb gap (depending on the electrostatic force and the quality factor) should be chosen.

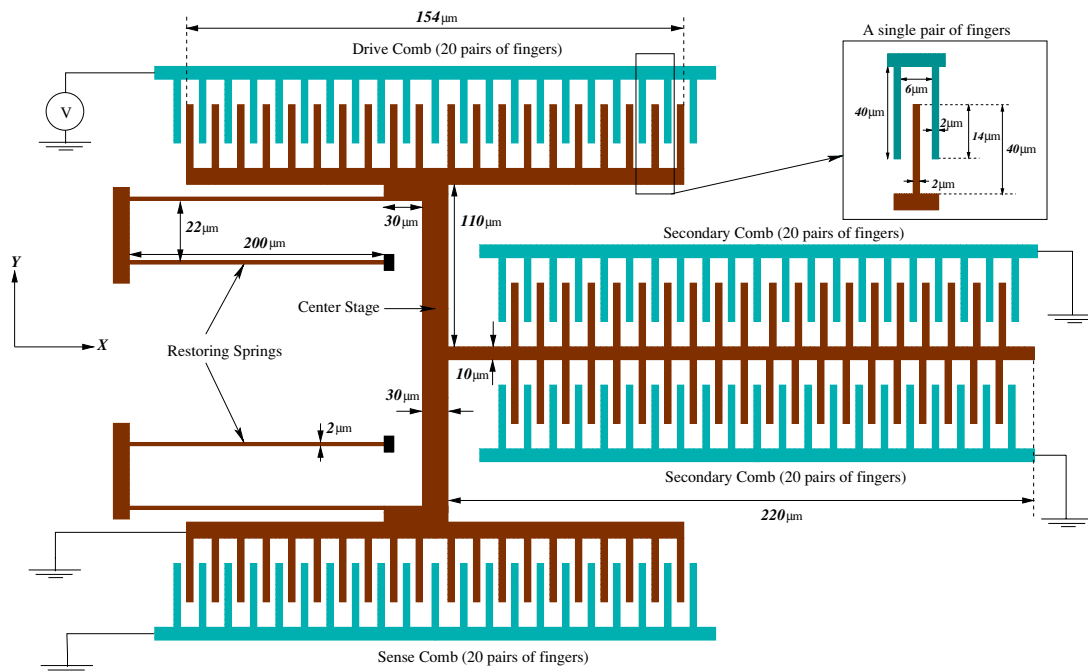


Figure 13. MEMS lateral comb drive [36]. The comb drive moves in the Y-direction.

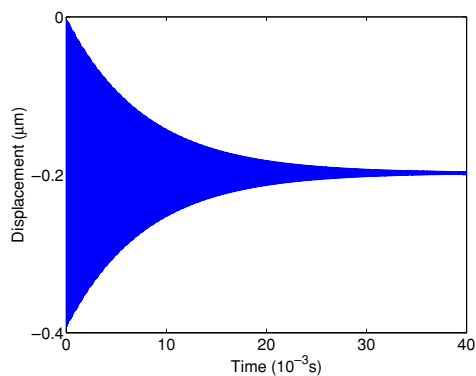


Figure 14. Damped transient response of the rigid center stage of the lateral comb drive at 25 V dc.

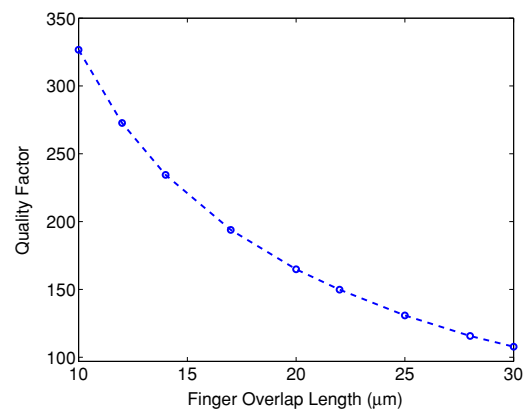


Figure 16. Variation of the quality factor with the finger overlap length in the lateral comb drive.

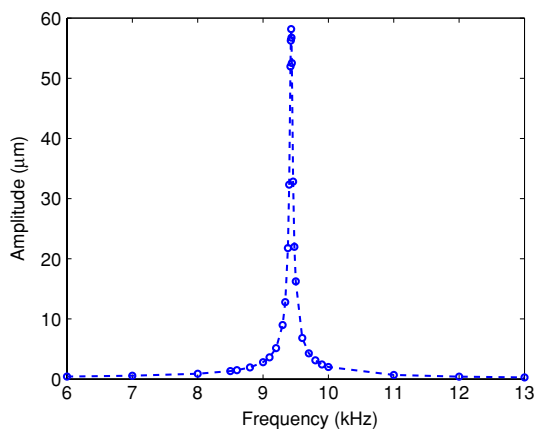


Figure 15. Frequency response of the lateral comb drive at 20 V dc and 10 V ac.

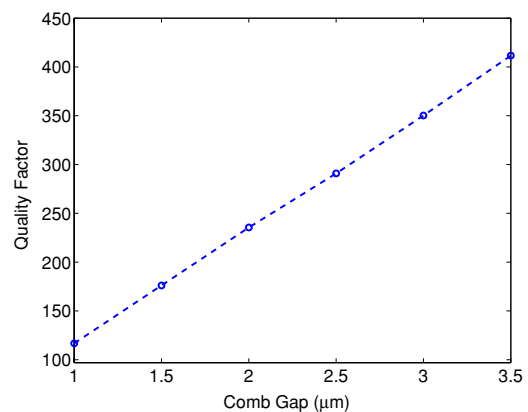
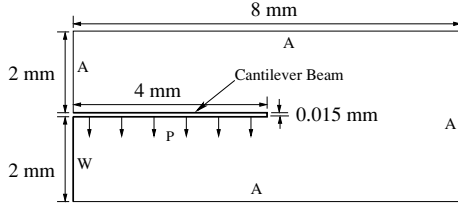
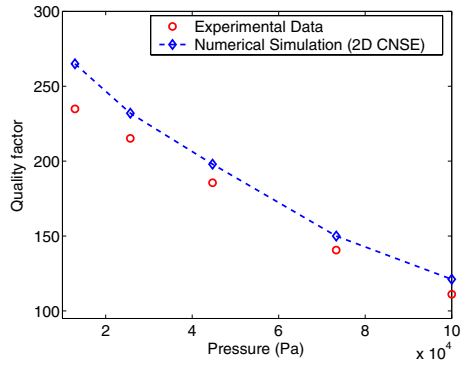


Figure 17. Variation of the quality factor with comb gap in the lateral comb drive.



**Figure 18.** The simulation domain for the cantilever beam vibrating in air [38] used in the 2D CNSE solver and the appropriate boundary conditions applied.  $W$  denotes walls where slip flow boundary conditions were applied for the fluid velocity and  $A$  denotes ambient conditions where the fluid pressure is set to the ambient pressure.  $P$  is the applied external pressure to the cantilever beam.



**Figure 19.** Variation in quality factor of the MEMS cantilever beam with ambient pressure obtained from experiments and from the 2D CNSE solver.

#### 4.4. Cantilever beam in air

MEMS cantilever beams vibrating in air in the absence of any ground plane below them have several applications such as a resonating force sensor or a resonating micro-bridge mass flow sensor [38]. The dynamics of such a MEMS cantilever beam 4000  $\mu\text{m}$  long, 500  $\mu\text{m}$  wide and 15  $\mu\text{m}$  thick vibrating in air [38] is simulated using the 2D CNSE solver for the fluidic analysis. The beam is made from silicon and has a Young's modulus  $E = 169$  GPa, density  $\rho = 2330$  kg  $\text{m}^{-3}$  and Poisson's ratio  $\nu = 0.3$ . In the experimental setup, the cantilever beam was excited by a mechanical exciter at its base. The peak displacement of the beam was kept low to avoid any form of nonlinearities in the oscillations. In the numerical simulations, the 2D CNSE solver coupled with the mechanical solver is used (no electrostatic analysis is involved). The cantilever beam is made to vibrate in air by applying a small external pressure  $P = 100 \sin(2\pi f_e t)$  N  $\text{m}^{-2}$  ( $f_e$  is the excitation frequency) to its bottom surface as shown in figure 18. The simulation domain used along with the appropriate boundary conditions applied in the 2D CNSE solver is also shown in figure 18. The excitation frequency  $f_e$  is swept for a given ambient pressure to obtain the quality factor and the resonant frequency at that pressure. Figures 19 and 20 show the variation in the quality factor and the resonant frequency  $f$ , normalized with respect to  $f_0$ , the resonant frequency in vacuum, of the beam with the ambient pressure. The viscosity of air is taken to be  $\eta = 1.82 \times 10^{-5}$  kg  $\text{m}^{-1} \text{s}^{-1}$  and the mean free path  $\lambda$  for air is computed from equation (12) at different pressures and at 293 K. While

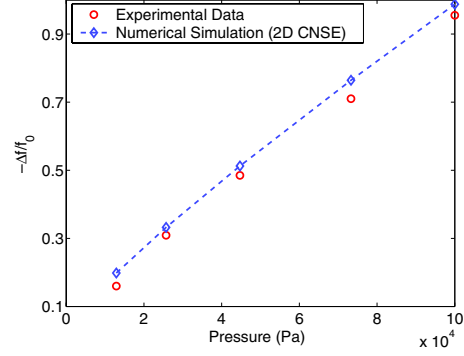


**Figure 20.** Variation in the resonant frequency of the MEMS cantilever beam with ambient pressure.  $\Delta f = f - f_0$ , where  $f$  and  $f_0$  are the resonant frequencies at the given ambient pressure and in vacuum, respectively.

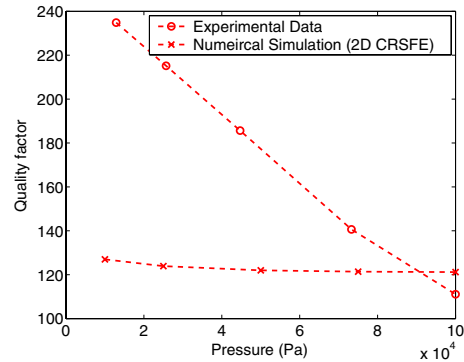


**Figure 21.** Variation in quality factor of the MEMS cantilever beam with ambient pressure obtained from experiments and from the 2D CRSFE solver.

the numerically simulated (using 2D CNSE) variation in the resonant frequency of the beam with the ambient pressure is close to the experimental data in figure 20, the measured quality factors at low pressures are found to be smaller than the values simulated by the 2D CNSE model in figure 19. This may be due to the fact that as the pressure reduces the fluid damping forces become smaller and other sources of damping in MEMS [39], such as anchor losses, thermoelastic damping, become significant for the cantilever beam. This would reduce the measured quality factor compared to the simulated value that is based only on fluid damping.

#### 4.5. Limitations of the Reynold's squeeze film damping model

The MEMS cantilever beam in air considered in section 4.4 is simulated in this section using the 2D CRSFE solver instead of the 2D CNSE solver. An imaginary ground electrode is placed close to the MEMS cantilever beam and the system is simulated using the coupled electro-mechanical–fluidic solver based on 2D CRSFE for the fluidic analysis. A small dc bias of 1 V along with a small ac voltage of 0.1 V is applied between the ground plane and the beam to keep the oscillations in the linear regime. Under normal atmospheric conditions, the quality factor of the beam with an imaginary ground electrode simulated using the 2D CRSFE model matches with that of the original system (cantilever beam in air simulated using

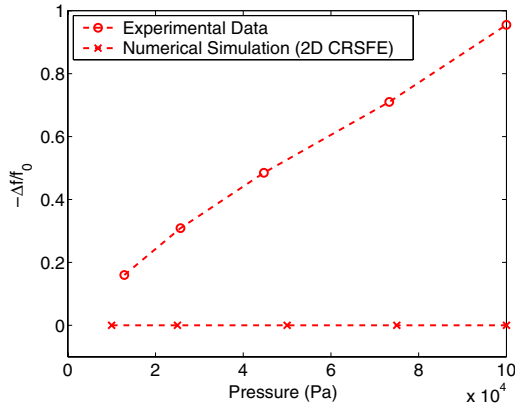


**Figure 22.** Variation in the resonant frequency of the MEMS cantilever beam with ambient pressure.  $\Delta f = f - f_0$ , where  $f$  and  $f_0$  are the resonant frequencies at the given ambient pressure and in vacuum, respectively.

the 2D CNSE model) for a gap of  $107 \mu\text{m}$  and the value is found to be 121. The variations in the quality factor and the resonant frequency (obtained using 2D CRSFE) of the beam with the imaginary ground plane at a gap of  $107 \mu\text{m}$  with the ambient pressure are plotted in figures 21 and 22. Figure 21 shows that 2D CRSFE predicts a much smaller change in the quality factor compared to the experimental data while figure 22 shows that 2D CRSFE predicts no change in the resonant frequency of the beam with ambient pressure. These observations are considerably different from the predictions of 2D CNSE (which is close to the experimental data as shown in figures 19 and 20) due to the improper application of the 2D CRSFE in this case ( $l/h$  is not large).

## 5. Conclusion

In this paper, we have presented a full-Lagrangian Newton method for the dynamic analysis of electrostatic MEMS in the presence of fluid damping. Two hierarchical fluid models, namely the compressible Reynold's squeeze film equation and the compressible Navier–Stokes equations, are coupled with electrostatic and mechanical models using a full-Lagrangian formulation and a Newton method with accurate computation of the Jacobian matrix for the coupling. Both these features make this method far more efficient than existing coupled electro-mechanical–fluidic solvers for the dynamic analysis of MEMS. The physical models are validated by simulating several complex MEMS devices and comparing important design parameters such as the resonant frequency and the quality factor obtained from the numerical simulation with experimental data. The coupling of the two hierarchical fluid models (the 2D CRSFE and the 2D CNSE) with the coupled electro-mechanical solver makes it possible to simulate the dynamics of a large class of MEMS devices. While the faster 2D CRSFE based solver can be used to accurately simulate certain classes of MEMS devices (having large aspect ratios and small gaps like the micromirror and the piggyback actuator), the more accurate and comparatively slower 2D CNSE based solver can be used for MEMS devices where 2D CRSFE is not valid, for example, the cantilever beam in air.

## Acknowledgments

This work is supported by the National Science Foundation under grant numbers 0121616, 0217986, 0228390 and 0601479.

## Appendix A. 2D compressible Reynold's squeeze film equation (CRSFE): time integration, numerical discretization and derivation of the Jacobian terms

From equation (11) and using the relations  $h = g + v$  and  $K = \lambda/h = \lambda/(g + v)$ , where  $g$  is the gap between the microstructure and the ground plane in the undeformed configuration and  $v$  is the displacement of the microstructure perpendicular to the ground plane (in the  $Y$ -direction in figure 1), the fluidic residual equation  $\mathbf{R}_F$  for the compressible Reynold's squeeze film equation (CRSFE) (equation (11)) can be written as

$$\mathbf{R}_F = 12\eta \frac{\partial}{\partial t} [P_f(v + g)] - f(P_f, u, v) = 0, \quad (\text{A.1})$$

where

$$\begin{aligned} f(P_f, u, v) &= \frac{\partial}{\partial X} \left[ \left\{ 1 + 6 \frac{\lambda}{(v + g)} \right\} (v + g)^3 P_f \frac{\partial P_f}{\partial X} \left( 1 + \frac{\partial u}{\partial X} \right)^{-1} \right] \\ &\quad \times \left( 1 + \frac{\partial u}{\partial X} \right)^{-1} + \frac{\partial}{\partial Z} \left[ \left\{ 1 + 6 \frac{\lambda}{(v + g)} \right\} (v + g)^3 P_f \frac{\partial P_f}{\partial Z} \right]. \end{aligned} \quad (\text{A.2})$$

The time integration of equation (A.1) is done using the Crank–Nicholson scheme [40] and is given by

$$\begin{aligned} \mathbf{R}_F^{n+1} &= 12\eta \frac{[P_f(v + g)]^{n+1} - [P_f(v + g)]^n}{\Delta t} \\ &\quad - \frac{1}{2} [f(P_f^{n+1}, u^{n+1}, v^{n+1}) + f(P_f^n, u^n, v^n)] = 0, \end{aligned} \quad (\text{A.3})$$

where the superscripts  $n + 1$  and  $n$  are used to denote the values of the variables at the time instants  $t^{n+1}$  and  $t^n$ , respectively, and  $\Delta t$  is the time step. In equation (A.3),  $P_f^{n+1}$ ,  $u^{n+1}$  and  $v^{n+1}$  are the unknowns to be evaluated at the time instant  $t^{n+1}$ , and  $P_f^n$ ,  $u^n$  and  $v^n$  are all known. Note that in the Newton method, since the electrical, mechanical and fluidic equations are solved simultaneously,  $u^{n+1}$  and  $v^{n+1}$  are also treated as unknowns in the fluidic equation. In this regard, equation (A.3) can be rewritten as

$$\mathbf{R}_F = 12\eta \frac{[P_f(v + g)]}{\Delta t} - \frac{1}{2} f(P_f, u, v) - R = 0, \quad (\text{A.4})$$

where the superscript  $n + 1$  has been dropped from the unknown variables at the time instant  $n + 1$  and  $R$  is a collection of all the terms that depend on the values of the variables at the time instant  $t^n$  only. The meshless finite cloud method (FCM) (see [17, 22, 23] for details on FCM) is used to solve equation (A.4). FCM uses a fixed-kernel technique to construct the interpolations functions and a point collocation technique to discretize the partial differential equations. In this method, the value of an unknown  $p$  at an arbitrary point  $(X_i, Z_i)$  in the discretized domain is given by the relation

$$\begin{aligned} p(X_i, Z_i) &= p_i \\ &= \sum_{j=1}^{\text{NP}} N_j(X_i, Z_i) \hat{p}_j, \quad i = 1, 2, \dots, \text{NP}, \end{aligned} \quad (\text{A.5})$$

where NP is the total number of points in the domain,  $N_j(X_i, Z_i)$  is the value of the meshless interpolation function for the point  $j$  at  $(X_i, Z_i)$  and  $\hat{p}_j$  is the nodal parameter for the variable  $p$  at the point  $j$ . After collecting the unknowns and the nodal parameters into a matrix form, the value of the unknown  $p$  at point  $i$  can be written as

$$p_i = \sum_{j=1}^{NP} [N]_{ij} \hat{p}_j, \quad (\text{A.6})$$

where  $[N]_{ij}$  represents  $N_j(X_i, Z_i)$ . The derivatives of the unknown can also be expressed in a similar manner, i.e.,

$$p = [N]\hat{p}, \quad p_{,X} = [NX]\hat{p}, \quad p_{,Z} = [NZ]\hat{p}, \quad (\text{A.7})$$

$$p_{,XX} = [NXX]\hat{p}, \quad p_{,ZZ} = [NZZ]\hat{p}, \\ p_{,XZ} = [NXZ]\hat{p}, \quad (\text{A.8})$$

where  $[NX]$ ,  $[NZ]$ ,  $[NXX]$ ,  $[NZZ]$  and  $[NXZ]$  are the matrices containing the  $X$ ,  $Z$ , second  $X$ , second  $Z$  and  $X$ - $Z$  derivatives of the interpolation functions, respectively (see [41] for more details). The spatial discretization of equation (A.4) is done by expressing the variables  $P_f$ ,  $u$  and  $v$  and their derivatives in terms of their nodal parameters  $\hat{P}_f$ ,  $\hat{u}$  and  $\hat{v}$ , respectively, using equation (A.8).

The Jacobian term  $\mathbf{R}_{FF}$  (an  $\text{NP} \times \text{NP}$  matrix in this case) can be computed from equation (A.4) as

$$(\mathbf{R}_{FF})_{ij} = \frac{\partial(\mathbf{R}_F)_i}{\partial(\hat{P}_f)_j} = 12\eta \frac{[v_i + g]}{\Delta t} [N]_{ij} \\ - \frac{1}{2} \frac{\partial f_i}{\partial(\hat{P}_f)_j}, \quad i, j = 1, 2, \dots, \text{NP}, \quad (\text{A.9})$$

where  $(\mathbf{R}_{FF})_{ij}$  is the term in the  $i$ th row and  $j$ th column of  $\mathbf{R}_{FF}$  and the expression  $\partial f_i / \partial(\hat{P}_f)_j$  from equation (A.2) is given by

$$\frac{\partial f_i}{\partial(\hat{P}_f)_j} = \frac{\partial}{\partial Z} \left[ \left\{ 1 + 6 \frac{\lambda}{(v_i + g)} \right\} (v_i + g)^3 \right. \\ \left. \times \left\{ (P_f)_i [NZ]_{ij} + \left( \frac{\partial P_f}{\partial Z} \right)_i [N]_{ij} \right\} \right. \\ \left. + \frac{\partial}{\partial X} \left[ \left\{ 1 + 6 \frac{\lambda}{(v_i + g)} \right\} (v_i + g)^3 \right. \right. \\ \left. \left. \times \left\{ (P_f)_i [NX]_{ij} + \left( \frac{\partial P_f}{\partial X} \right)_i [N]_{ij} \right\} \right. \right. \\ \left. \left. \times \left\{ 1 + \left( \frac{\partial u}{\partial X} \right)_i \right\}^{-1} \right] \times \left\{ 1 + \left( \frac{\partial u}{\partial X} \right)_i \right\}^{-1} \right]. \quad (\text{A.10})$$

Note that the nodal parameters of the unknown variables are solved for in the FCM formulation instead of the nodal values of the unknown variables. Hence, the Jacobian matrix has derivatives with respect to the nodal parameters of the unknown variables instead of the unknown variables directly. The Jacobian term  $\mathbf{R}_{FM}$  is given by

$$(\mathbf{R}_{FM})_{ij} = \begin{Bmatrix} \frac{\partial(\mathbf{R}_F)_i}{\partial \hat{u}_j} \\ \frac{\partial(\mathbf{R}_F)_i}{\partial \hat{v}_j} \end{Bmatrix}^T = \begin{Bmatrix} -\frac{1}{2} \frac{\partial f_i}{\partial \hat{u}_j} \\ 12\eta \frac{(P_f)_i}{\Delta t} [N]_{ij} - \frac{1}{2} \frac{\partial f_i}{\partial \hat{v}_j} \end{Bmatrix}^T, \quad (\text{A.11})$$

where the derivatives of  $f_i$  with respect to  $\hat{u}_j$  and  $\hat{v}_j$  can be computed in a similar manner as in equation (A.10) from equation (A.2). The effect of fluidics on mechanics (i.e., the computation of the term  $\mathbf{R}_{MF}$ ) enters as a boundary

condition through equation (13) into the mechanical analysis. The mechanical residual equation at the microstructure–fluid interface/boundary  $\mathbf{R}_{M(\text{boundary})}$  from equations (3) and (13) can be written as

$$\mathbf{R}_{M(\text{boundary})} = \mathbf{H} - \mathbf{P} \cdot \mathbf{N} = J(P_e - P_{fe}) \mathbf{F}^{-T} \mathbf{N} - \mathbf{P} \cdot \mathbf{N}. \quad (\text{A.12})$$

$\mathbf{R}_{MF}$  can be computed from equation (A.12) as

$$(\mathbf{R}_{MF})_{ij} = \frac{\partial(\mathbf{R}_M)_i}{\partial(\hat{P}_f)_j} \\ = \begin{cases} -J_i \frac{\partial(P_{fe})_i}{\partial(\hat{P}_f)_j} \mathbf{F}_i^{-T} \mathbf{N}_i, & \text{if } i \in \text{boundary,} \\ 0, & \text{otherwise.} \end{cases} \quad (\text{A.13})$$

## Appendix B. 2D compressible Navier–Stokes equations (CNSE): time integration, numerical discretization and derivation of the Jacobian terms

From equations (17)–(20), the fluidic residual equations,  $\mathbf{R}_F$ , for the compressible Navier–Stokes equations (CNSE) can be written as

$$\mathbf{R}_F = \frac{\partial \mathbf{D}}{\partial t} + \mathbf{E} = 0, \quad (\text{B.1})$$

where

$$\mathbf{D} = \{\rho_f J_f \quad \rho_f J_f u_f \quad \rho_f J_f v_f \quad A \quad B \quad L \quad M\}^T, \quad (\text{B.2})$$

$\mathbf{E} =$

$$\begin{Bmatrix} -\frac{\partial}{\partial X}(u_f M - v_f L) - \frac{\partial}{\partial Y}(v_f A - u_f B) \\ \frac{\partial}{\partial X}(P_f M - \sigma_{xx} M + \tau_{xy} L) + \frac{\partial}{\partial Y}(-P_f B + \sigma_{xx} B - \tau_{xy} A) \\ \frac{\partial}{\partial X}(-P_f L - \tau_{yx} M + \sigma_{yy} L) + \frac{\partial}{\partial Y}(P_f A + \tau_{yx} B - \sigma_{yy} A) \\ -\frac{\partial u_f}{\partial X} \\ -\frac{\partial v_f}{\partial X} \\ -\frac{\partial u_f}{\partial Y} \\ -\frac{\partial v_f}{\partial Y} \end{Bmatrix}. \quad (\text{B.3})$$

The time integration of equation (B.1) is done using the Crank–Nicholson scheme and is given by

$$\mathbf{R}_F^{n+1} = \frac{\mathbf{D}^{n+1} - \mathbf{D}^n}{\Delta t} + \frac{1}{2}[\mathbf{E}^{n+1} + \mathbf{E}^n] \\ = \frac{\mathbf{D}^{n+1}}{\Delta t} + \frac{1}{2}\mathbf{E}^{n+1} - \mathbf{R}^n = 0, \quad (\text{B.4})$$

where the notation used is similar to that in appendix A and  $\mathbf{R}^n$  is a collection of all the terms that depend on the values of the variables at the time instant  $t^n$  only. Equation (B.4) can be rewritten as

$$\mathbf{R}_F = \frac{\mathbf{D}}{\Delta t} + \frac{1}{2}\mathbf{E} - \mathbf{R} = 0, \quad (\text{B.5})$$

where the superscripts  $n+1$  and  $n$  have been dropped and  $\mathbf{R}$  is independent of the unknown variables at the time instant  $t^{n+1}$ . The finite cloud method is used to solve equation (B.5). Equation (A.8) is used to express the unknown variables,  $\mathbf{x}_F = \{\rho_f, u_f, v_f, A, B, L, M\}^T$ , and their derivatives in terms of their nodal parameters given by  $\hat{\mathbf{x}}_F = \{\hat{\rho}_f, \hat{u}_f, \hat{v}_f, \hat{A}, \hat{B}, \hat{L}, \hat{M}\}^T$ .

The Jacobian term,  $\mathbf{R}_{FF}$  (a  $7NP \times 7NP$  matrix in this case), can be computed from equation (B.5) as

$$\begin{aligned} (\mathbf{R}_{FF})_{ij} &= \frac{\partial(\mathbf{R}_F)_i}{\partial(\hat{\mathbf{x}}_F)_j} \\ &= \frac{1}{\Delta t} \frac{\partial \mathbf{D}_i}{\partial(\hat{\mathbf{x}}_F)_j} + \frac{1}{2} \frac{\partial \mathbf{E}_i}{\partial(\hat{\mathbf{x}}_F)_j}, \quad i, j = 1, 2, \dots, NP. \end{aligned} \quad (\text{B.6})$$

From equation (B.2) and using the relation  $J = \det(\mathbf{F}_f) = AM - BL$

$$\begin{aligned} \frac{\partial \mathbf{D}_i}{\partial(\hat{\mathbf{x}}_F)_j} &= \\ & \left[ \begin{array}{ccccccc} J_f & 0 & 0 & \rho_f M & -\rho_f L & -\rho_f B & \rho_f A \\ J_f u_f & \rho_f J_f & 0 & \rho_f M u_f & -\rho_f L u_f & -\rho_f B u_f & \rho_f A u_f \\ J_f v_f & 0 & \rho_f J_f & \rho_f M v_f & -\rho_f L v_f & -\rho_f B v_f & \rho_f A v_f \\ 0 & 0 & 0 & 1 & 0 & 0 & 0 \\ 0 & 0 & 0 & 0 & 1 & 0 & 0 \\ 0 & 0 & 0 & 0 & 0 & 1 & 0 \\ 0 & 0 & 0 & 0 & 0 & 0 & 1 \end{array} \right]_i [N]_{ij}. \end{aligned} \quad (\text{B.7})$$

Similarly,  $\partial \mathbf{E}_i / \partial(\hat{\mathbf{x}}_F)_j$  can be computed from equation (B.3). The mechanical to fluidic and fluidic to mechanical coupling terms of the Jacobian matrix are only present at the solid (microstructure)–fluid interface in this case. At the solid–fluid interface, the solid (microstructure) velocity is transferred to the fluid through the slip flow correction (equation (24)). As a result, equations (17), (24) (instead of equations (18) and (19)) and (20) are solved for the fluid domain at the solid–fluid interface and form the set of residual equations  $\mathbf{R}_F$  in this case. The Jacobian term,  $\mathbf{R}_{FM}$  (a  $7NP \times 2NP$  matrix in this case), can be written as

$$(\mathbf{R}_{FM})_{ij} = \frac{\partial(\mathbf{R}_F)_i}{\partial(\hat{\mathbf{x}}_M)_j} = \left\{ \begin{array}{c} \frac{\partial(\mathbf{R}_F)_i}{\partial \hat{u}_j} \\ \frac{\partial(\mathbf{R}_F)_i}{\partial \hat{v}_j} \end{array} \right\}^T. \quad (\text{B.8})$$

The relations between the structural velocities  $\dot{u}$  and  $\dot{v}$  and the structural displacements  $u$  and  $v$  (see [14]) and equation (24) are used to compute the terms  $\partial(\mathbf{R}_F)_i / \partial \hat{u}_j$  and  $\partial(\mathbf{R}_F)_i / \partial \hat{v}_j$  in equation (B.8). The fluidic stress  $\mathbf{T}_f$  computed from the fluidic analysis is transferred to the mechanical analysis through equations (3) and (25) and forms the mechanical residual equation at the microstructure–fluid interface/boundary  $\mathbf{R}_{M(\text{boundary})}$  in this case, i.e.,

$$\begin{aligned} \mathbf{R}_{M(\text{boundary})} &= \mathbf{H} - \mathbf{P} \cdot \mathbf{N} \\ &= J [P_e \mathbf{I} + \mathbf{T}_f] \mathbf{F}^{-T} \mathbf{N} - \mathbf{P} \cdot \mathbf{N}. \end{aligned} \quad (\text{B.9})$$

The Jacobian term,  $\mathbf{R}_{MF}$  (a  $2NP \times 7NP$  matrix in this case), can be written as

$$\begin{aligned} (\mathbf{R}_{MF})_{ij} &= \frac{\partial(\mathbf{R}_M)_i}{\partial(\hat{\mathbf{x}}_F)_j} \\ &= \begin{cases} J_i \frac{\partial(\mathbf{T}_f)_i}{\partial(\hat{\mathbf{x}}_F)_j} \mathbf{F}_i^{-T} \mathbf{N}, & \text{if } i \in \text{boundary,} \\ 0, & \text{otherwise,} \end{cases} \end{aligned} \quad (\text{B.10})$$

where  $\partial(\mathbf{T}_f)_i / \partial(\hat{\mathbf{x}}_F)_j$  can be computed in a similar manner as equation (B.7) from equation (16).

## References

[1] Karniadakis G E, Beskok A and Aluru N R 2005 *Microflows and Nanoflows: Fundamentals and Simulation* (New York: Springer)

- [2] Luo H, Fedder G K and Carley R 2000 A 1 mG lateral CMOS-MEMS accelerometer *IEEE Proc. MEMS'00* pp 502–7
- [3] Juneau T, Pisano A P and Smith J H 1997 Dual axis operation of a micromachined rate gyroscope *Int. Conf. on Solid-State Sensors and Actuators—Transducers '97* pp 883–6
- [4] Yazdi N, Ayazi F and Najafi K 1998 Micromachined inertial sensors *Proc. IEEE* **86** 1640–59
- [5] Senturia S D 1998 CAD challenges for microsensors, microactuators, and microsystems *Proc. IEEE* **86** 1611–26
- [6] Hung E S and Senturia S D 1999 Generating efficient dynamical models for microelectromechanical systems from a few finite-element simulation runs *J. Microelectromech. Syst.* **8** 280–9
- [7] Schrag G and Wachutka G 2002 Physically based modeling of squeeze film damping by mixed-level system simulation *Sensors Actuators A* **97–98** 193–200
- [8] Pan F, Kubby J, Peeters E, Tran A T and Mukherjee S 1998 Squeeze film damping effects on the dynamic response of a MEMS torsion mirror *J. Microelectromech. Syst.* **8** 200–8
- [9] Ye W, Wang X, Hemmert W, Freeman D and White J 2003 Air damping in laterally oscillating microresonators: a numerical and experimental study *J. Microelectromech. Syst.* **12** 557–66
- [10] Turowski M, Chen Z and Prezekwas A 1999 High-fidelity and behavioral simulation of air damping in MEMS *Proc. Int. Conf. on Modeling and Simulation of Microsystems—MSM'99* pp 241–4
- [11] Senturia S D, Aluru N R and White J 1997 Simulating the behavior of MEMS devices: computational methods and needs *IEEE Comput. Sci. Eng.* **4** 30–43
- [12] Aluru N R and White J 1997 An efficient numerical technique for electromechanical simulation of complicated microelectromechanical structures *Sensors Actuators A* **58** 1–11
- [13] Aluru N R and White J 1999 A multi-level Newton method for mixed-energy domain simulation of MEMS *J. Microelectromech. Syst.* **8** 299–308
- [14] De S K and Aluru N R 2004 Full-Lagrangian schemes for dynamic analysis of electrostatic MEMS *J. Microelectromech. Syst.* **13** 737–58
- [15] Li G and Aluru N R 2003 Efficient mixed-domain analysis of electrostatic MEMS *IEEE Trans. Comput.-Aided Des. Integr. Circuits Syst.* **22** 1228–42
- [16] Mukherjee S, Bao Z, Roman M and Aubry N 2005 Nonlinear mechanics of MEMS plates with a total Lagrangian approach *Comput. Struct.* **83** 758–68
- [17] Jin X, Li G and Aluru N R 2005 New approximations and collocation schemes in the finite cloud method *Comput. Struct.* **83** 1366–85
- [18] Li G and Aluru N R 2003 A boundary cloud method with a cloud-by-cloud polynomial basis *Eng. Anal. Bound. Elem.* **27** 57–71
- [19] Starr J B 1990 Squeezed-film damping in solid-state accelerometers *Technical Digest: Proc. Solid-State Sensor and Actuator Workshop* pp 44–7
- [20] Chandrasekharaiah D S and Debnath L 1994 *Continuum Mechanics* (New York: Academic)
- [21] Bathe K J 1995 *Finite Element Procedures* (Englewood Cliffs, NJ: Prentice-Hall)
- [22] Aluru N R and Li G 2001 Finite cloud method: a true meshless technique based on a fixed reproducing kernel approximation *Int. J. Numer. Methods Eng.* **50** 2373–410
- [23] Jin X, Li G and Aluru N R 2004 Positivity conditions in meshless collocation methods *Comput. Methods Appl. Mech. Eng.* **193** 1171–202
- [24] Li G and Aluru N R 2002 A Lagrangian approach for electrostatic analysis of deformable conductors *J. Microelectromech. Syst.* **11** 245–54
- [25] Li G and Aluru N R 2002 Boundary cloud method: a combined scattered point/boundary integral approach for

- boundary-only analysis *Comput. Methods Appl. Mech. Eng.* **191** 2337–70
- [26] Burgdorfer A 1959 The influence of the molecular mean free path on the performance of hydrodynamic gas lubricated bearings *Trans. ASME, J. Basic Eng.* **81** 94–1000
- [27] Veijola T, Kuisma H, Lahdenpera J and Ryhanen T 1995 Equivalent-circuit model of the squeezed gas film in a silicon accelerometer *Sensors Actuators A* **48** 239–48
- [28] Vincenti W G and Kruger C H 1967 *Introduction to Physical Gas Dynamics* (New York: Wiley)
- [29] Hirt C W, Amsden A A and Cook J L 1974 An arbitrary Lagrangian–Eulerian computing method for all flow speeds *J. Comput. Phys.* **14** 227–317
- [30] Hui W H 2004 A unified coordinates approach to computational fluid dynamics *J. Comput. Appl. Math.* **163** 15–28
- [31] Després B and Mazeran C 2003 Symmetrization of Lagrangian gas dynamics in dimension two and multidimensional solvers *C. R. Mec.* **331** 475–80
- [32] Gupta R K 2000 Electronically probed measurements of MEMS geometries *J. Microelectromech. Syst.* **9** 380–9
- [33] Toshiyoshi H, Mita M and Fujita H 2002 A MEMS piggyback actuator for hard-disk drives *J. Microelectromech. Syst.* **11** 648–54
- [34] Varadan V K, Varadan V V and Subramanian H 2001 Fabrication, characterization and testing of wireless MEMS-IDT based microaccelerometers *Sensors Actuators A* **90** 7–19
- [35] Imamura T, Katayama M, Ikegawa Y, Ohwe T, Koishi R and Koshikawa T 1998 MEMS-based integrated head/actuator/slider for hard disk drives *IEEE/ASME Trans. Mechatronics* **3** 166–74
- [36] Hang Z and Tang W C 1994 Viscous air damping in laterally driven microresonators *IEEE Proc. MEMS'94* pp 199–204
- [37] Rosa M A, Dimitrijevic S and Harrison H B 1998 Improved operation of micromechanical comb-drive actuators through the use of a new angled comb finger design *J. Intell. Mater. Syst. Struct.* **9** 283–90
- [38] Blom F R, Bouwstra S, Elwenspoek M and Fluitman J H J 1992 Dependence of the quality factor of micromachined silicon beam resonators on pressure and geometry *J. Vac. Sci. Technol. B* **10** 19–26
- [39] Candler R N, H Li, Lutz M, Park W-T, Partridge A, Yama G and Kenny T W 2003 Investigation of energy loss mechanisms in micromechanical resonators *Int. Conf. on Solid-State Sensors and Actuators—Transducers '03* pp 332–5
- [40] Tannehill J C, Anderson D A and Pletcher R H 1997 *Computational Fluid Mechanics and Heat Transfer* (London: Taylor and Francis)
- [41] Mitchell M J, Qiao R and Aluru N R 2000 Meshless analysis of steady-state electro-osmotic transport *J. Microelectromech. Syst.* **9** 435–49